ACS OMEGA

Open Access

http://pubs.acs.org/journal/acsodf

Article

Sensitization of Europium Oxide Nanoparticles Enhances Signal-to-Noise over Autofluorescence with Time-Gated Luminescence Detection

Hunter A. Miller, Jessica Q. Wallace, Hui Li, Xing-Zhong Li, Ana de Bettencourt-Dias, and Forrest M. Kievit*

Cite This: *ACS Omega* 2024, 9, 31093−31104

Read Online

ACCESS | Metrics & More | Article Recommendations | Supporting Information

ABSTRACT: Clinical translation of nanoparticle-based therapeutics has been limited, and a lack of preclinical delivery characterization is partly to blame, limiting our understanding of the mechanisms of failure. The improvement of the preclinical delivery assessment requires nanoparticles with higher detectability. This work focused on the exploration of several aromatic carboxylic ligands (terephthalic acid, quinaldic acid, and kynurenic acid) for the sensitization of europium oxide nanoparticles with a long emission lifetime to overcome cellular autofluorescence, a key confounder of detection in luminescence-based bioimaging. A facile one-pot synthesis and ligand exchange process generated and sensitized ultrasmall Eu_2O_3 cores. As reflected in the emission spectra and lifetimes, ligand binding yielded unique coordination environments around Eu^{3+}. Then, the efficacy of sensitization was tested against the autofluorescence provided by tissue lysate. Normal (simultaneous excite-read) measurements showed integrated signal improvements over autofluorescence of 2.2-, 3.9-, and 14.0-fold for EuTA, EuQA, and EuKA, respectively. In time-gated mode, the improvements over autofluorescence were more dramatic with fold differences of 75-, 89-, and 108-fold for EuTA, EuQA, and EuKA, respectively. The investigation of novel sensitizers expands the breadth of the field of sensitized lanthanide oxide nanoparticles, and the signal enhancement observed with sensitization and time-gating supports the utility of the generated samples for future bioimaging applications.

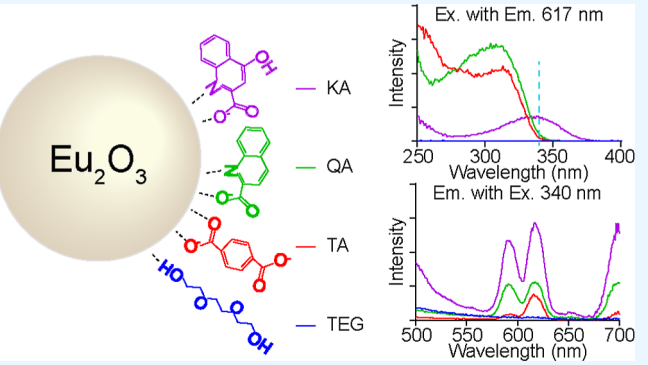

1. INTRODUCTION

Nanoparticles (NPs) are well suited to various drug delivery problems; given the variety of physicochemical properties, they can assume and the resulting pharmacokinetic behavior.[1−4] Previous preclinical work in conditions including stroke and traumatic brain injury has shown improved delivery and outcomes through the use of NP-based therapeutics.[5−7] Drug delivery in these conditions is severely complicated by the blood−brain barrier, but pathologic changes in its function offer opportunity, particularly with NP-based therapeutics.[8−10] Clinical translation has been limited as more robust characterization of preclinical delivery including pharmacokinetics and (sub)cellular localization is needed to better understand target engagement and improve predictions of clinical efficacy. This characterization, however, is dependent on improving the NP detectability. Studies commonly rely on exogenous fluorescent dyes conjugated to the NP surface to facilitate their detection. This strategy has proven useful but is ultimately limited by fluorophore dissociation, photobleaching, and emissions on the same time scale as biological autofluorescence.[11,12] NP systems with native luminescence, such as ultrasmall lanthanide oxides and quantum dots,[13−15] can circumvent these issues in preclinical use. While luminescence microscopy offers adequate spatial resolution for describing cellular localization, autofluorescence hinders the detection of exogenous signals. To overcome this, several strategies have been employed. Methods have focused on different procedural steps including staining and image processing, in the forms of electromagnetic or chemical quenching pretreatments and spectral unmixing algorithms, respectively.[16,17] Others have approached the issue through material design, with organic and inorganic nanomaterials that fluoresce or excite in the first or second biological transparency windows.[18] A final approach has been the development of materials whose emission lifetimes extend beyond the ps to ns range of most autofluorescence.[19] The development of such luminescent NPs with long excited state

Received: May 10, 2024
Revised: May 24, 2024
Accepted: June 14, 2024
Published: July 2, 2024

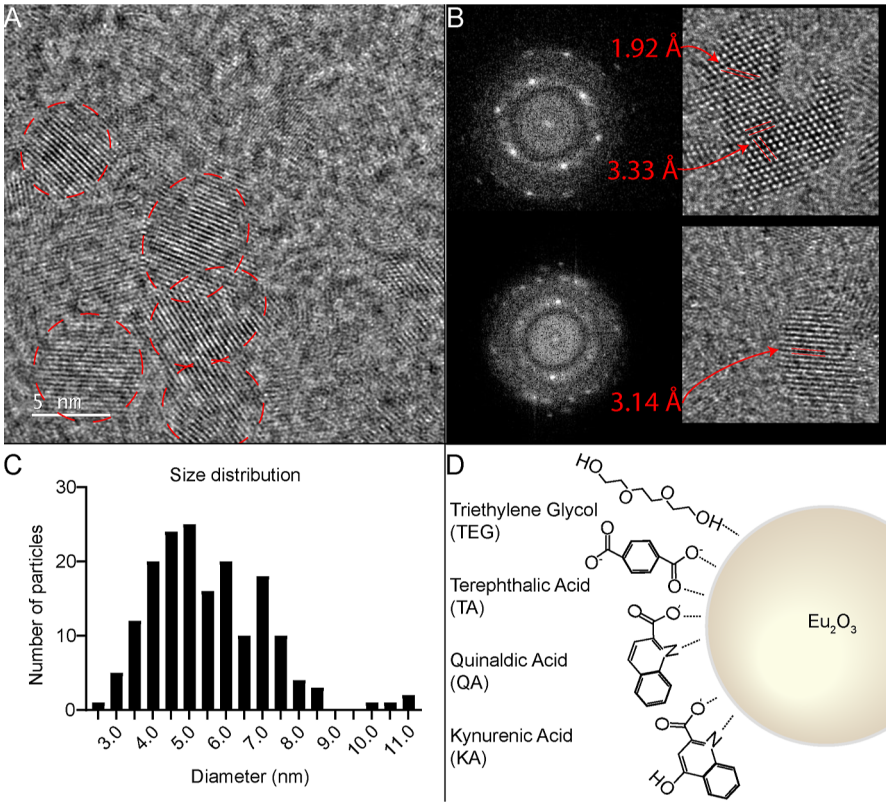

Figure 1. High-resolution TEM of EuTEG NPs (A) shows lattice fringes characteristic of crystallinity. Fast Fourier transform of NPs along distinct zone axes (B) further shows the crystalline nature of NPs. A sample of roughly 150 NPs was used to generate a core size distribution (C). Ligands coordinate with the surface of the Eu cores; one potential orientation of each ligand is shown (D). Of note, different sensitizing ligands were not used in combination; the aim of the diagram is to show ligand structure and putative localization at the NP surface.

lifetimes may be combined with time-gated imaging to provide a more accurate and sensitive understanding of the cellular distribution of the NPs.

Several ions in the lanthanide series exhibit excited state lifetimes on the order of μs to ms, related to the forbidden nature of their intra 4f transitions.[20] The long lifetimes and narrow emission lines, particularly those of Eu and Tb, have been leveraged to yield highly sensitive immunoassays for biomarkers of cancer and other conditions.[21,22] Time-resolved assays can substantially increase signal-to-noise ratio (SNR), lowering detection limit, and required sample volumes, and increasing throughput.[23] Other lanthanides exhibit upconversion luminescence, which can enhance detectability through minimization of background signal and increased tissue penetration using near-infrared wavelengths.[24] The forbidden 4f transitions that provide longer emission lifetimes have the drawback of low molar absorptivity, below 1 M^{-1} cm^{-1}, within the series. Yb^{3+} is an exception with a partially allowed transition with absorption at 980 nm, motivating its use as a dopant sensitizer in upconverting NPs. The low absorptivities the lanthanide series exhibit can be overcome via the antenna effect, in which a sensitizing molecule absorbs energy and transfers it to the lanthanide ion.[23] Organic sensitizing ligands commonly exhibit molar absorptivities orders of magnitude larger than lanthanide ions, in the range of 10^3 to 10^5 M^{-1} cm^{-1}.[25] Small-molecule Eu complexes have been prepared with various sensitizers including bipyridine and terpyridine derivatives,[26,27] as well as aromatic carboxylates.[28,29] In addition to small-molecule chelates, Eu has been used as a majority component or dopant in inorganic NPs including oxides and fluorides, limiting metal−solvent interactions.[30−34] Compared with Eu^{3+}, the sensitization of upconverting $NaGdF_4$ NPs with surface-bound ligands has only more recently been investigated, with applications including bioimaging, optogenetics, and photovoltaics.[25,35−37] In the realm of bioimaging, ligand-sensitized rare earth sesquioxide NPs (e.g., Eu_2O_3), though present in the literature, have not been nearly as widely explored as small-molecule compounds.[38,39] Yet, they present advantages including control over physicochemical properties like size and surface chemistry, cargo loading potential, higher absorption per unit contrast agent, protection of emitters from high-energy oscillators, and potential for doping with multiple ions for multiplexing applications.[37,40] Further investigation is therefore needed to more fully realize the potential of such sensitized particulate systems in bioimaging applications to help in the preclinical evaluation of nanomedicines to accelerate their clinical translation.

A suitable sensitizer will efficiently absorb and transfer energy to Eu centers while limiting nonradiative losses during energy transfer (ET). These losses are related to factors including the relative energy levels of donor−acceptor excited states and the number of water molecules coordinated to Eu, as the high energy O−H oscillators quench the lanthanide-centered emission.[41,42] The hard acid behavior of Eu and other lanthanides yield effective binding with hard base ligands, frequently involving multiple oxygen−lanthanide bonds in small molecule chelates.[43] Species with carboxyl groups have been used as surface agents for inorganic lanthanide NPs, commonly oleic, citric, and D-glucuronic acids, as the acid self-

https://doi.org/10.1021/acsomega.4c04457
ACS Omega 2024, 9, 31093−31104

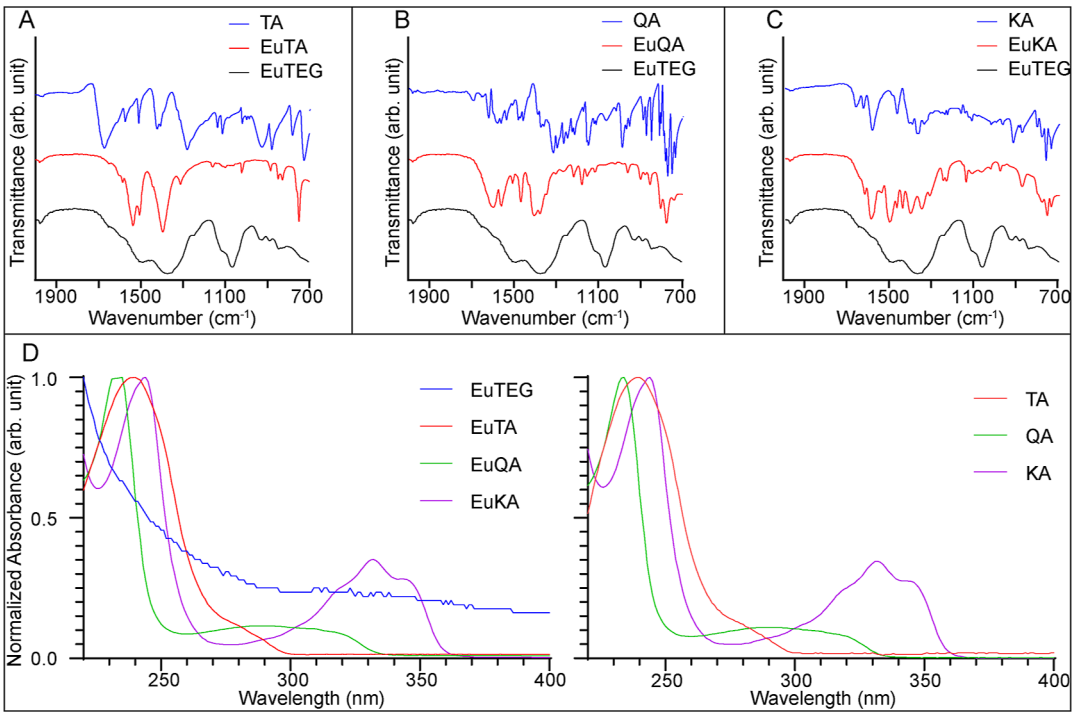

Figure 2. ATR-IR spectroscopy confirms the presence of ligands on the NP surface based on peak shifts from the pure ligand spectra as well as differences from the EuTEG spectrum. (A–C) UV–vis spectroscopy was used to measure the absorbance of NPs and free ligand in solution. (D) The normalized absorbance spectra of NPs closely resemble those of the respective free ligands, corroborating successful ligand exchange.

assembles on the surface through bidentate or bridging modes.[44] Dipicolinic acid has been used to sensitize Eu^{3+} emission, but there are limited alternative options for ligand sensitization without unwieldy synthetic protocols.[45] The sensitization of Eu_2O_3 NPs for bioimaging is underexplored in the literature, and the surface binding of carboxyl groups represents an established coordination strategy with promise to enhance luminescence detectability.

In this work, a low-temperature one-pot polyol method was used to produce sesquioxide NPs, and sensitization was performed via ligand exchange to one of several aromatic carboxylates: terephthalic acid (TA), quinaldic (2-quinoline-carboxylic) acid (QA), and kynurenic acid (KA), which were compared against the control capping agent triethylene glycol (TEG). These were chosen as simple molecules that may offer expanded excitation options in sensitized Eu NPs. TA was previously explored in other NP systems,[46−48] while QA showed efficacy in chelates,[49] and KA was yet undescribed for the sensitization of Eu^{3+}. The core structure of the NPs was analyzed with transmission electron microscopy (TEM), while the ligand-surface binding and luminescence effects were analyzed with attenuated total reflectance infrared (ATR-IR) spectroscopy, ultraviolet–visible (UV–vis) spectroscopy, phosphorescence spectroscopy, and phosphorescence lifetime measurements. The samples were then imaged in solution with tissue lysate to incorporate cellular autofluorescence using normal and time-gated collection modes as a proof-of-concept use case to show high detectability.

2. RESULTS AND DISCUSSION

2.1. Core Synthesis and Characterization. A modified polyol method was used to synthesize ultrasmall Eu_2O_3 NPs. The high boiling point alcohol, in this case TEG, served as both solvent and capping agent for the nanocrystals. TEM study revealed ultrasmall, roughly spherical crystals with an average core diameter of 5.5 nm (Figure 1A,C). Fast Fourier transform and quantification of lattice spacing of selected crystals confirmed the expected body-centered cubic (BCC) structure of Eu_2O_3 (Figure 1B), with prominent planes including (220), (221), and (224), with plane spacing of approximately 3.33, 3.14, and 1.92 Å, respectively. Inductively coupled plasma mass spectroscopy (ICP-MS) verified Eu presence in the NP samples. These combined data confirmed the generation of Eu_2O_3 nanocrystals in the desired ultrasmall size range with the expected BCC crystal structure.

2.2. Ligand Exchange. Ligand exchange to sensitize the emission of Eu(III) was performed following the validation of the core synthesis. Three aromatic carboxylic acids, TA, QA, and KA were chosen for this purpose. Previous work in lanthanide oxides has shown self-assembly of carboxyl-based ligands on the NP surface.[44] The ligand exchange protocol consisted of adding the ligand to the EuTEG solution at 60 °C and stirring overnight under an argon flow. Unreacted ligand and other precursors were then removed via dialysis. The expected surface coordination schemes of TEG and the 3 sensitizing ligands are shown in Figure 1D. ATR-IR spectroscopy was used to assess the surface-bound ligand on the NPs (Figure 2A–C). The presence of TA was confirmed on the NP by the appearance of the peaks at 1537 and 1585 cm^{-1}, which correspond to the carboxylate.[50] QA was confirmed on the NP surface by the peak at 1596 cm^{-1}, corresponding to the benzene ring and carboxyl of the ligand. KA on the NP was confirmed based on a similar benzene–carboxyl peak at 1593 cm^{-1} as well as the peak at 1505 cm^{-1} related to aromatic carbon–carbon double bonds.[51] The ATR-IR spectra of sensitized NPs were seen to be distinct from that of EuTEG (black line Figure 2A–C) indicating that the ligand exchange process was successful and TEG capping was replaced by the

https://doi.org/10.1021/acsomega.4c04457
ACS Omega 2024, 9, 31093−31104

desired ligands. TEM study of NPs after ligand exchange and dialysis showed similar core sizes (Figure S2). Dynamic light scattering of the NP samples showed the formation of aggregates (Figure S3), which motivated future work to improve colloidal stability.

To test how surface coordination of ligands affected NP optical properties, UV−vis absorbance spectroscopy was performed on samples of free ligand as well as control and ligand-sensitized NPs suspended in phosphate-buffered saline (PBS) at pH 7.4 (Figure 2D). At this pH value, these three ligands existed in their anionic base forms. EuTEG showed an increasing absorbance as the wavelength decreased, with λ_{max} at 220 nm, the lower bound of our absorbance measurement. EuTEG exhibited a sharp decrease as wavelength increased up to about 250 nm, after which the decline slowed but continued. Free TA and EuTA showed similar spectra with a maximum of around 240 nm and a shoulder near 280 nm. Free QA showed a peak at 232 nm (λ_{max}) and a broad peak centered near 290 nm. EuQA was highly similar to a peak at 235 nm (λ_{max}) and the same broad peak near 290 nm. Free KA and EuKA both showed a peak near 248 nm (λ_{max}), with a broader, smaller peak at 332 nm. The presence of similar strong absorption peaks in free ligand and ligand-sensitized NPs indicates that TEG was displaced by a sensitizer at the NP surface during the ligand exchange.

The experimentally observed UV−vis absorption spectra were well reproduced and explained by TD-CAMB3LYP calculations of these ligands in their aqueous solvated anionic base forms (Figure S1, Tables 1 and S1). It is well known that

Table 1. Comparison of Measured and Calculated Absorbance Peaks

sensitizing ligand	experimental absorbance peak wavelengths (nm)	corrected TD-CAMB3LYP absorbance peak wavelengths (nm)
TA	240, 280	265, 280
QA	232, 290	243, 310
KA	248, 332	250, 326

TD-CAMB3LYP tends to overestimate excitation energies, typically by ∼0.5 eV. Here, a −0.5 eV correction is applied to all TD-CAMB3LYP calculated singlet excited state energies.

The excitation energies and intensities for each species (anion and water molecules, Figure S1) were computed for only one molecular geometry that was identified as the global minimum with the MMFF94 force field method and subsequently optimized with B3LYP method (in the gas phase) on the S_0 ground state potential energy surface. In reality, a large number of low-lying dynamic structures exist that can contribute to the experimentally measured UV−vis absorption spectrum. The fact that the calculated absorption energies (after −0.5 eV correction) and intensities are close to experimental maximum values suggests that the geometries used in the calculations are among the most probable hydrogen bonding network geometries for the anions and the first layer of solvent water molecules around the carboxylate groups. After binding to the surface of the NPs, these ligands exhibited almost identical UV−vis absorption spectra (Figure 2D), implying that they remained in anionic base forms, and their carboxylate groups were well solvated by water molecules.

UV−vis was also used to determine the amount of ligand bound to the 3 sensitized NPs. NPs were dissolved and fitted to standard curves. NP number concentration was estimated based on EuTEG core size, the density of Eu_2O_3, and ICP-MS ion concentration values. Quantified ligand loads were 1759, 4216, and 3274 ligands per particle of EuTA, EuQA, and EuKA respectively. On a per surface area basis, these values become 18.5, 44.4, and 34.4 molecules/nm^2 for EuTA, EuQA, and EuKA, respectively.

2.3. Sensitization Effect on Luminescence. Following confirmation of the sensitizing ligand at the NP surface, the effect on the luminescence was investigated. The excited state energy levels of sensitizers were calculated, and details are given in the Methods section. Energy levels are shown relative to the $^5D_J \rightarrow {}^7F_{J'}$ ($J = 0-1$, $J' = 0-3$) transitions of Eu in a Jablonski diagram (Figure 3). While work in small molecule

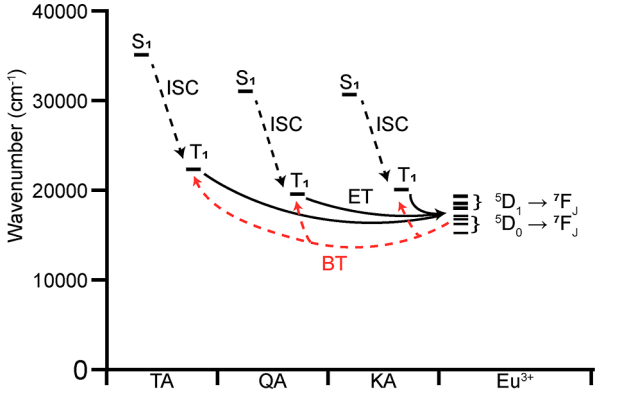

Figure 3. Jablonski diagram of excited states in sensitizing ligands calculated via density functional theory. Excited singlet states can populate excited triplet states via intersystem crossing (ISC). ET processes move energy from ligand-excited triplet (T_1) states to Eu^{3+} excited states from which the characteristic radiative emission can then occur. Back transfer (BT) from Eu^{3+} to the ligand can occur when the T_1 state energy levels are too close to those of the Eu^{3+}, limiting emission. Details on computations can be found in the Methods section.

chelates has often focused on the energy difference between the lowest triplet excited state (T_1) and the emissive state of Eu,[52,53] there is also evidence for excitation of Eu and other lanthanides via the singlet state or higher lying triplet states.[54−57] The calculated T_1s of TA, QA, and KA (in their anionic base forms), ranging from 19,575 to 22,366 cm^{-1} (footnotes of Tables S2.2, S2.4, S2.6), were all above the $^5D_0$ and $^5D_1$ states of Eu^{3+}, which lie near 17,200 and 19,350 cm^{-1} respectively.[58] Though the high-resolution elucidation of ET processes is beyond the scope of this work, the calculated energy levels suggest that $T_1 \rightarrow {}^5D_{0/1}$ is likely the predominant pathway in the tested systems. The calculated T_1s indicated that the ligands were generally well suited to sensitize Eu based on Latva's empirical rule, which indicates that efficient ET would be expected for an energy gap of roughly 2000−4000 cm^{-1}.[52,59] More recent data suggests that optimal T_1 levels for efficient ET to Eu^{3+} should lie in the range of 19,532−21,740 cm^{-1},[53] which the ligands fit with the exception of TA that lies just above that upper bound. The calculations also indicated T_1 should be efficiently populated by intersystem crossing within the ligands, based on Reinhoudt's empirical rule which suggests an energy gap greater than 5000 cm^{-1} between the lowest singlet excited state (S_1) and T_1.[60,61] Luminescence excitation and emission spectra (Figure 4 top row) and intensity decay curves (Figure 4 bottom row) were collected

https://doi.org/10.1021/acsomega.4c04457
ACS Omega 2024, 9, 31093−31104

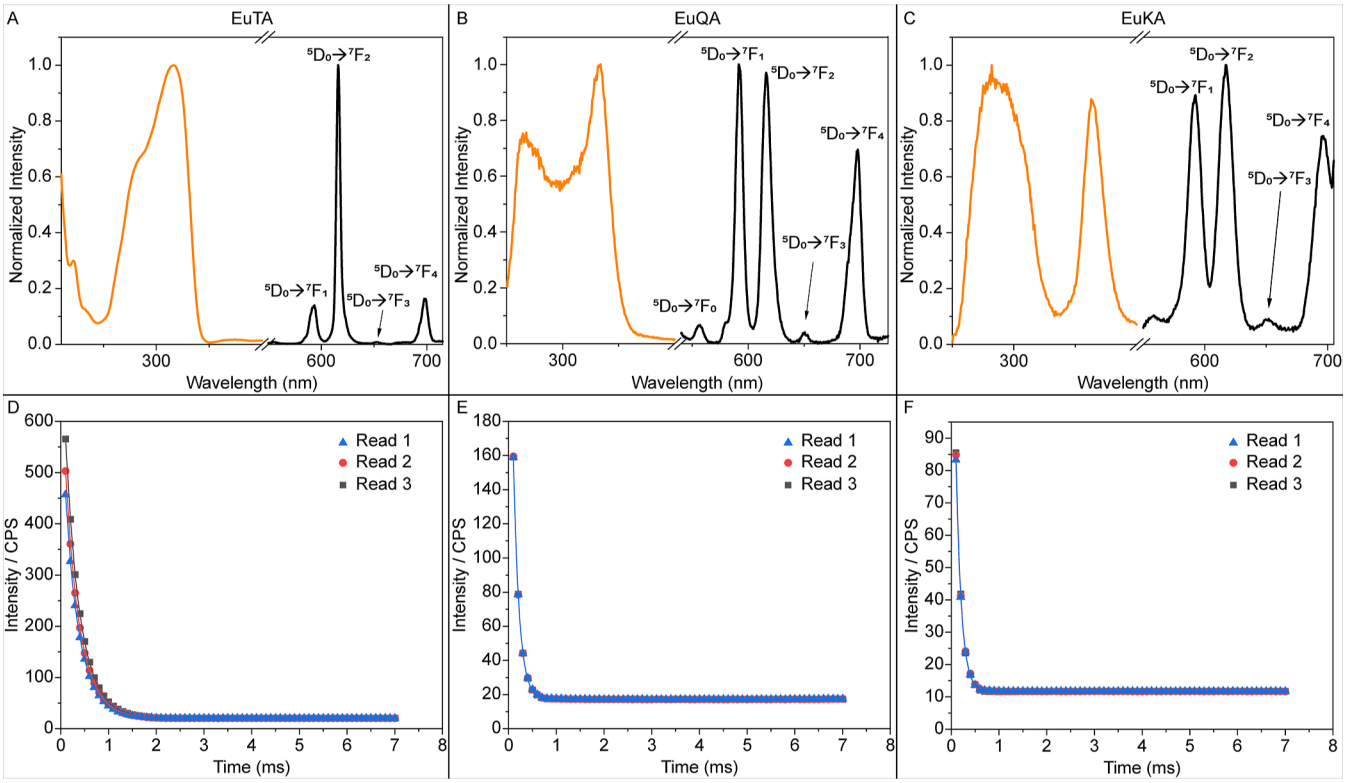

Figure 4. (A–C) Normalized excitation (orange) and emission (black) spectra of sensitizer-capped Eu NPs (0.05 mM Eu^{3+}). (D–F) Intensity decay curves (three independent trials) of the $^5D_0 \rightarrow {}^7F_2$ transition (617 nm) from the same samples. Excitation spectra were recorded at emission wavelength 617 nm. Emission spectra were collected with excitation at 327, 334, and 363 nm for EuTA, EuQA, and EuKA, respectively. Excitation and emission slit widths were respectively 10 and 4 nm for EuTA, 10 and 5 nm for EuQA, and 10 and 9 nm for EuKA.

for all of the NPs in water. In EuTEG no Eu emission was seen regardless of excitation wavelength. Even direct excitation of the Eu ion at 395 nm ($^7F_0 \rightarrow {}^5L_6$) did not yield any metal-centered emission. This is not surprising, as TEG itself does not have any significant absorption that could sensitize the Eu emission, and the molar absorptivity of the $^7F_0 \rightarrow {}^5L_6$ is rather low, $\varepsilon < 10\ M^{-1}\ cm^{-1}$.[62] Moreover, the presence of multiple Eu centers in close proximity can facilitate energy migration to surface quenching sites, limiting luminescence.[63] Doped Gd_2O_3 and Y_2O_3 systems often show luminescence intensity peaks with 10% Eu-doping or less, exhibiting quenching at higher concentrations. The Eu_2O_3 NPs here have more concentrated Eu centers, comparatively, which may yield more substantial quenching.[30,64] Passivation of the surface with an inert inorganic layer or a ligand has been shown to help limit such quenching, but TEG is not effective in this function.[65]

Sensitization enabled detectable luminescence with each of the three ligands, despite the range of T_1 energy levels. Interestingly, the synthesis atmosphere was shown to be an important variable. Syntheses under argon showed substantially higher emission from Eu^{3+} transitions at 593 and 617 nm with sensitization than syntheses under air (Figure S4). The excitation spectrum of EuTA (Figure 4A) showed one broad band, with a maximum at 327 nm. This was red-shifted with respect to the absorption spectrum, which had a peak at 240 nm and shoulder at 280 nm, but the similar but broadened shape led us to conclude that the organic ligand sensitized the Eu-centered emission. The emission spectrum showed the characteristic $^5D_0 \rightarrow {}^7F_J$ ($J = 1–4$) transitions in the red region of the visible spectrum. The peak at 617 nm, corresponding to the electric dipole $^5D_0 \rightarrow {}^7F_2$ transition, was more intense than that at 593 nm, corresponding to the magnetic dipole $^5D_0 \rightarrow {}^7F_1$ transition, indicating a low degree of symmetry around the Eu centers.[66] The electric dipole transition is hypersensitive to the local environment of luminescent centers, while the magnetic dipole transition is independent of ligand field.[67−69] The ratio of the electric to magnetic transition emission intensities, R_1, has been employed as a metric of the symmetry of the Eu center, with higher values indicating lower symmetry.[70] The profile of this spectrum was quite different from the ones for QA- and KA-capped NPs, indicating a different geometry for the surface Eu^{3+} ions.

The emission decay lifetimes τ of EuTA were 123.9 and 323.2 μs (Table 2), as the decay curve was fitted with a double exponential (Figure 4D), which gave better results than fitting to a single exponential, as indicated by residuals and statistical parameters (Figures S5 and S6). The two lifetimes indicate two coordination environments around the Eu^{3+} ion;[71−73] the longer lifetime corresponds to 85.8% of the sites and will, necessarily, correspond to a site with decreased nonradiative

Table 2. Lifetime τ of the Eu $^5D_0$ Excited State in the Different Samples

sensitizing ligand	τ_1 (μs)	τ_2 (μs)
TA	123.9 ± 9.1 (14.2%)[a]	323.2 ± 3.8 (85.8%)[a]
QA	120.5 ± 0.1	
KA	111.6 ± 0.7	

[a]Percentage population of the site calculated as the normalized pre-exponential factors.

https://doi.org/10.1021/acsomega.4c04457
ACS Omega 2024, 9, 31093−31104

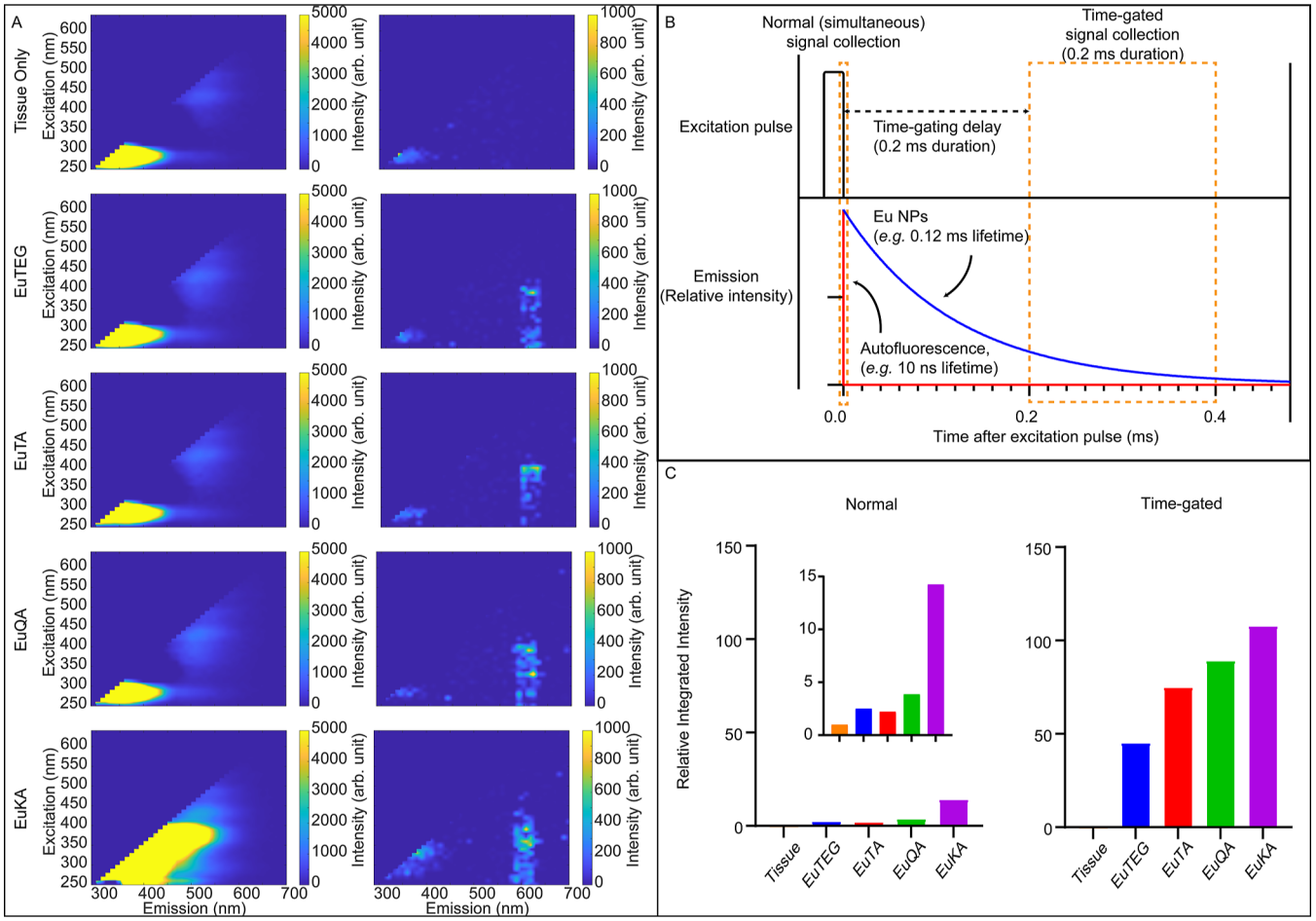

Figure 5. Excitation−emission matrices (A) of tissue-spiked NPs collected in simultaneous (left) and time-gated (right) modes with a 0.2 ms delay. The time−course diagram (B) shows the conceptual rationale for using the time-gated rather than simultaneous read mode to detect Eu over short-lived autofluorescence originating from tissue. Integrated signal intensity plots (C) show fold increases in NP signal relative to tissue noise in time-gated reads versus simultaneous. Signal was integrated over excitation wavelengths from 300 to 400 nm and emission from 590 to 640 nm. The Eu^{3+} concentration was 0.05 mM for all samples, and the tissue concentration was 100 μg/mL.

quenching. QA and KA are monocarboxylic acid sensitizers and have the potential for N,O-hybrid coordination.[74] TA, on the other hand, is a dicarboxylic acid without N. The two carboxylate functional groups presented the opportunity for different coordination modes.[29,42,48,75−77] The double exponential fit provided further evidence of the different coordination environments for TA initially suggested by the lower ligand density relative to QA and KA.

The excitation spectrum of EuQA (Figure 4B) showed bands with maxima at 264 and 334 nm. Like the EuTA, the excitation spectrum was red-shifted compared to the absorption spectrum, which had bands at 235 and 290 nm, leading us to conclude that the capping ligand sensitized the Eu-centered emission. The emission spectrum showed characteristic Eu^{3+}-centered emission bands for the $^5D_0 \rightarrow {}^7F_J$ (J = 0−4) transitions in the red region of the visible spectrum. This system's most intense peak corresponded to the $^5D_0 \rightarrow {}^7F_1$ transition, and R_1 was just below 1. These points suggest the possible presence of an inversion center,[78,79] while the presence of the $^5D_0 \rightarrow {}^7F_0$ transition suggests a low symmetry environment. As the most intense transition for the TA-capped system was the $^5D_0 \rightarrow {}^7F_2$ transition, R_1 was much greater than 1, and the $^5D_0 \rightarrow {}^7F_0$ transition was not observed; we concluded that the Eu^{3+} ions were in different coordination environments in each system.[41,42]

The emission decay lifetime τ of EuQA was 120.5 μs (Table 2). The decay curve was fitted with a single exponential decay (Figures 4E and S7), consistent with one coordination environment around the Eu^{3+} ion.[42]

The excitation spectrum of EuKA (Figure 4C) showed a broader and a narrower band with maxima at 282 and 363 nm, respectively, consistent with sensitization of the Eu-centered emission through the capping ligand. Compared with the peaks of the absorption spectrum near 248 and 332 nm, we saw a redshift of the maxima of 34 and 31 nm, respectively. We believe that the ligand coordination with the metal increased its planarity, causing the redshift.[80−82] A similar redshift in excitation relative to absorption was seen in lanthanide nanoparticles sensitized with dipicolinic acid.[45] When excited at 363 nm, EuKA nanoparticles emitted in the red region of the visible spectrum, and the characteristic metal-centered emission peaks of the $^5D_0 \rightarrow {}^7F_J$ (J = 1−4) transitions were observed. The R_1 of this system was slightly greater than 1, indicating a distinct Eu coordination environment compared with that of EuTA and EuQA.

The emission decay lifetime τ of the Eu-centered emission of EuKA was 111.6 μs (Table 2). The decay curve was fitted with

https://doi.org/10.1021/acsomega.4c04457
ACS Omega 2024, 9, 31093−31104

a single exponential decay (Figures 4F and S8), consistent with one coordination environment around the Eu^{3+} ion.[41,42]

Table 1 summarizes the lifetimes of the studied sensitizer-capped NPs described above. EuTA exhibited the longest lifetime, while EuKA had the shortest lifetime. In addition, EuTA showed a dual lifetime decay. As TA was the only dicarboxylic ligand employed, it was supposed that this enabled the formation of two coordination environments, with the longer-lived component corresponding to a site with less nonradiative decay.

Zhao and co-workers synthesized Eu complexes that contained the TA sensitizer as well as other ligands, including 2-thienyltrifluoroacetonate and trioctylphosphine oxide; they exhibited lifetimes from 0.46 to 0.52 ms.[48] These complexes were bi− and polynuclear, as TA is a common bridging ligand, which accounted for the long lifetimes observed. Xiaochun and co-workers synthesized zinc-, chromium-, and cadmium-doped Eu complexes containing the TA sensitizer that exhibited lifetimes from 0.35 to 0.38 ms.[83]

In Eu NPs, investigators have seen a range of emission lifetimes in various media (i.e., solid state or in aqueous solutions).[84−88] Irfanullah and co-workers synthesized sensitizer-capped Eu-doped LaF_3 nanocrystals with an average Eu emission lifetime of 0.41 ms.[84] We observed shorter lifetimes in this work, likely because our measurements were in water, while the reported values for the LaF_3 nanocrystals were measured in the solid state. The tetracycline-capped Eu-doped carbon nanoparticles synthesized by Pacheco and co-workers exhibited a double exponential decay with lifetimes of 0.0796 and 0.174 ms.[85] They were attributed to two different environments for the Eu^{3+} ions with the longer lifetime coming from the Eu^{3+} ions protected from the surroundings. Similarly, we saw a turn-on in luminescence in this work upon the addition of the capping ligands, as they replaced the water molecules at the nanoparticle surface. Adusumalli and co-workers obtained a double exponential decay with lifetimes of 2.17 and 6.43 ms for TA-capped Eu-doped nanoparticles.[86] These long lifetimes were measured in aqueous media; interestingly, quenching from the presence of the O−H vibrations was not discussed. Atrazine-capped Eu_2O_3 particles synthesized by Feng and co-workers exhibited a Eu emission lifetime of ∼100 μs.[87] Hybrid Eu^{3+} and silica nanoparticles isolated by Zhang and co-workers exhibited a lifetime of 0.98 ms, which was longer than the emission lifetime of 0.42 and 0.74 ms of the non-nanoparticle-supported Eu complexes.[88] This was attributed to the rigid covalent Si−O−Si network, which inhibited ligand vibrations that could quench lanthanide emission. The lifetime values observed in this work fell within the range expected, although consistently toward the shorter end. However, the comparison of lifetimes is complicated by the inconsistency of the medium used in different works, which strongly influences quenching.[42] Ligands can limit solvent quenching by passivating surface ions to a degree, but discrepancies in system synthesis and measurement conditions between papers still complicate comparison. Along with passivation, ligands can affect lifetime through the presence of high-energy oscillators, as shown in the work of Varaksina et al.[89] By replacing 2C−H bonds in a β-diketonate with C−F, which is a lower frequency oscillator, they increased luminescence lifetime from 0.18 to 0.70 ms. Further increasing the fluorination yielded a lifetime of 0.96 ms. A final factor to mention in the emission lifetimes is concentration quenching, with reports from Rastogi et al. and Khudoleeva et al. showing shorter Eu^{3+} emission lifetimes at higher doping ratios.[90,91] We thus attributed the shorter lifetimes here to several factors including poor surface passivation, concentration quenching, and nonradiative decay through high-energy oscillators.[42,89−91] Nonetheless, the novel ligands tested here add breadth to the literature regarding the sensitization of nanoparticulate Eu.

2.4. Time-Gated Imaging and Autofluorescence Interference. To test the sensitizer-capped NPs in an environment with cellular autofluorescence, solutions were prepared containing NPs and brain tissue lysate in PBS. The samples were then examined in a fluorescence plate reader in both normal and time-gated read modes. Excitation−emission matrices were collected with excitation from 250 to 640 nm, emission from 300 to 700 nm, and a step size of 10 nm. The normal, simultaneous excitation−emission matrices (Figure 5A left) show roughly similar appearance across conditions with the exception of EuKA, which shows strong ligand-based luminescence in the range of excitation 300−400 nm with emission 400−500 nm. Emissions from the expected Eu transitions around 600 nm were not especially clear, though integrating emission intensities from 590 to 640 nm over excitation from 300 to 400 nm showed a higher signal in NPs than tissue alone (Figure 5C left). The NP-tissue intensity ratios for EuTEG, EuTA, EuQA, and EuKA were 2.5, 2.2, 3.9, and 14.0, respectively. Samples were also collected in time-gated mode with a 200 μs delay, allowing the decay of short-lived autofluorescence and the capture of long-lived Eu luminescence (Figure 5B). Time-gated matrices (Figure 5A right) revealed discernible Eu emission lines around 600 nm in all NPs and a lower autofluorescence signal. EuTEG, EuTA, EuQA, and EuKA showed NP-tissue intensity ratios of 45, 75, 89, and 108, respectively. The difference between EuTEG and the sensitized NPs, particularly with time-gating, showed the efficacy of surface sensitization to increase NP detectability related to autofluorescence. Notably, EuTEG showed signals with a time-gated collection that were undetectable in the phosphorescence excitation and emission spectra. This was likely related to differences between the instruments and protocols used in data collection as well as the dilute presence of species capable of sensitizing Eu in the buffer used for tissue lysate preparation, such as ethylene glycol-bis(2-aminoethyl ether)-*N*,*N*,*N*′,*N*′-tetraacetate (EGTA).[92]

3. CONCLUSIONS

TEG-coated Eu_2O_3 NPs were synthesized via a modified polyol route. Though no emission was observed for the control NPs, ligand exchange with TA, QA, or KA and sensitization via these ligands enabled the detection of the expected Eu^{3+} transitions. EuQA and -KA showed $^5D_0 \rightarrow {}^7F_1$ and $^5D_0 \rightarrow {}^7F_2$ peaks with similar intensities, while the $^5D_0 \rightarrow {}^7F_1$ transition of EuTA was less intense than the $^5D_0 \rightarrow {}^7F_2$ transition. The differences in emission profiles suggest different coordination environments around the Eu^{3+} ion. Another point of distinction was in the biexponential emission decay of EuTA, suggesting two unique environments within the system, unlike EuQA and EuKA, which showed monoexponential decay. The NPs showed drastic signal-to-autofluorescence noise improvements with ligand sensitization and time-gated imaging. These results support the utility and further investigation of ligand-sensitized Eu_2O_3 NPs for bioimaging applications to achieve high-sensitivity detections.

https://doi.org/10.1021/acsomega.4c04457
ACS Omega 2024, 9, 31093−31104

4. EXPERIMENTAL SECTION

4.1. Chemicals. Triethylene glycol (TEG, 99%), europium-(III) nitrate pentahydrate ($Eu(NO_3)_3{\cdot}5H_2O$, 99.9%), KA, QA, and TA were purchased from Sigma-Aldrich. Sodium hydroxide (NaOH) was purchased from Fisher. Float-A-Lyzer G2 dialysis devices were purchased from VWR.

4.2. Nanoparticle Synthesis. 60 mL TEG was stirred in a 250 mL three-necked flask equipped with a reflux condenser under argon flow. To the TEG at room temperature, 2 mmol of $Eu(NO_3)_3{\cdot}5H_2O$ was added, followed by 6 mmol of NaOH. The solution was gradually heated and then held at 90−100 °C for complete dissolution of the solid precursors. After dissolution, the flask was kept at 140 °C for 1 h. The temperature was then increased to 180 °C at a rate of about 5 °C/min and maintained there for 4 h. The light brown solution was then cooled to room temperature overnight. This solution was then dialyzed for the control EuTEG or used further for ligand exchange.

4.3. Ligand Exchange. Ligand exchange was performed to sensitize the nanoparticles with the desired surface groups. One mL of undialyzed solution from the above synthesis was added to a test tube followed by 2 mmol of either TA, QA, or KA. The solution was stirred under argon flow and held at 60 °C overnight (∼12 h) in a silicon oil bath. After ligand exchange, the solution was cooled to room temperature and thereafter stored at 4 °C.

4.4. Nanoparticle Washing. Directly following synthesis, for EuTEG, or after ligand exchange, for EuTA, EuQA, and EuKA, samples were washed via dialysis using Float-A-Lyzer G2 devices with a molecular weight cutoff of 3.5−5 kDa. Dialysis served to remove unreacted precursors from the synthesis as well as excess sensitizer from the ligand exchange. Samples were dialyzed against deionized water with a ratio of 1:2000 maintained over 24−36 h with water exchanged at least 3 times. Samples were then recovered from the dialysis devices and used for characterization.

4.5. Characterization. Inductively coupled plasma-mass spectrometry (Agilent 7500 cx) was performed on dialyzed samples to determine the Eu concentration. High-voltage TEM (Fei Tecnai Osiris (S)TEM, 200 keV) was used to measure the core size and assess the crystal structure of the NPs. Undialyzed EuTEG was diluted 1:30 in ethanol and drop cast on a lacey carbon-coated copper grid (PELCO mesh size 400, TED PELLA, INC). Image processing was performed using Landyne software suite and ImageJ.[93−95]

Attenuated total reflection infrared spectroscopy (Nicolet AVATAR 380 FT-IR) was performed on dried NP samples to verify the surface coordination of ligands. Dry NP samples were prepared by centrifugation of aqueous dispersions and resuspension of pellets in acetone before being dried in air. UV−vis absorbance spectra were collected on NP suspensions in PBS at pH 7.4 and a Eu^{3+} concentration of 0.05 mM. Absorbance spectra of free ligand were collected following dispersal in suitable solvents. TA was dissolved in DMSO and then diluted roughly 24,000× in PBS; KA was dissolved in 0.1 M NaOH and then diluted more than 1000× in PBS, while QA was dissolved directly in PBS. The absorbance spectra presented were normalized to their individual peak values in the range of 220−400 nm.

The electronic singlet excitation energies of the ligands in aqueous solution were calculated with the time-dependent density functional theory (TDDFT) method.[96−98] Since the pH was controlled at 7.4, these ligands existed in their anionic base forms (kynurenate, quinaldate, and terephthalate). To correctly describe the water hydrogen bonding effects on the electronic structures of these anions, water molecules were included in the calculation (Figure S1). Eight water molecules were included for kynurenate and for quinaldate, as they have one negatively charged carboxylate group. Sixteen water molecules were included for terephthalate, as it has two carboxylate groups. The anion-water clusters were first modeled with the MMFF94 force field,[99−102] and their global minimum structures were identified using the MDOPT scheme.[103] In the MDOPT calculation, a molecular dynamics (MD) simulation at 300 K was run for 10 ns. At every picosecond, the MD was paused, but not interrupted, for a steepest descendent geometry optimization to locate a minimum-energy structure. For the small molecules involved in this study, a 10 ns MD simulation was sufficient for finding the true global minimum. The identified global minimum structures were then geometrically optimized with the B3LYP[104] density functional theory method and the SPK-ADZP[105] basis set on the potential energy surfaces of both the singlet ground state (S_0) and the first triplet excited state (T_1). For the S_0 electronic ground state, closed shell (RHF) wave functions were used. For the T_1 electronic state, the spin-unrestricted open shell (UHF) wave functions were used and no significant spin contaminations were observed. Based on the six optimized molecular structures, TDDFT calculations were performed to estimate the low-lying singlet and triplet excited state energies and oscillator strengths. In the TDDFT calculations, the CAMB3LYP[106] density functional and the SPK-ADZP basis set were used. The aqueous solvent effect (in addition to the explicit water molecules in hydrogen bonding with the ligand molecules) was included in the TDDFT calculation with the FixSol[107] continuum solvation model with an electronic dielectric constant 1.777, which is the square of the refractive index 1.333 of pure water. It is well known that TD-CAMB3LYP tends to overestimate the singlet excited state energies of aromatic molecules.[108,109] To obtain better estimations for S_0 to S_n excitation energies, a straightforward −0.5 eV correction was applied to all calculated singlet excited state energies. The TD-CAMB3LYP also tends to predict triplet state energies that are slightly higher (by roughly +0.04 eV; see Table S1) than the corresponding singlet states. While in some cases, a triplet state can indeed have slightly higher energy than its singlet partner, this is not the case here. Therefore, this is a systematic and severe error of the TD-CAMB3LYP method for triplet states of the species in this work. To obtain more realistic estimation, the T_1 state energies were instead calculated with restricted open shell (ROHF with spin multiplicity = 3) CAMB3LYP wave function and the FixSol continuum solvation model with an electronic dielectric constant 1.777, and the S_0 state energies were calculated with closed shell (RHF with spin multiplicity = 1) CAMB3LYP wave function and the FixSol continuum solvation model with the same electronic dielectric constant 1.777. These S_0 and T_1 CAMB3LYP single-point energy calculations were performed with the gas phase spin-UHF B3LYP-optimized T_1 geometries. The results are presented as footnotes of Tables S2.2, S2.4, and S2.6. The calculations were performed with the General Atomic and Molecular Electronic System (GAMESS) quantum chemistry software package[110] and the QuanPol program,[111] which was integrated in the GAMESS package.

https://doi.org/10.1021/acsomega.4c04457
ACS Omega 2024, 9, 31093−31104

The emission and excitation spectra were measured on a PerkinElmer Lambda LS-55 instrument equipped with a 450 W xenon lamp. The data were collected in phosphorescence mode with a 0.1 ms delay, 0.1 ms gate time, and 20 ms cycle time. Excitation and emission slit widths varied and are indicated in the captions of the figures. Lifetimes were measured in phosphorescence mode with a 0.01 ms delay, 0.01 ms gate, and 20 ms cycle time. Unless otherwise indicated, all excitation and emission spectra and lifetimes were measured at 25.0 ± 0.1 °C. The data presented are the averages of at least three independent measurements.

The excitation−emission matrices were collected with a microplate reader (Synergy H1, BioTek). End point reads were performed from excitation wavelengths of 250−640 nm and emission wavelengths of 300−700 nm with steps of 10 nm. Samples were prepared by diluting NPs to 0.05 mM Eu^{3+} with tissue at 100 μg/mL in PBS. Data collection was performed in simultaneous excited-read mode and in time-gated mode with a 0.2 ms delay and 0.2 ms gate.

4.6. Tissue Lysate Preparation. Naïve male C57BL/6J mice (N = 3) were humanely euthanized following their completion of a separate study via perfusion with PBS at 80 mmHg. Following perfusion, brains were harvested, separated into two hemispheres, and homogenized using bead disruption with the TissueLyser II (Qiagen) in 300 μL of RIPA buffer (50 mM Tris HCl pH 8.0, 150 mM NaCl, 1% Triton X-100, 0.5% Na deoxycholate, 0.1% SDS, 1 mM EOTA, 0.5 mM EGTA, 1 mM PMSF, 1 mM Na_3VO_4, 1 mM NaF). Samples were sonicated using a horn sonicator for 20 s at 20% pulse frequency and centrifuged at 4 °C for 5 min at 17,740 rcf. Supernatants were collected, and total protein content was measured using a bicinchoninic acid (BCA) assay. Aliquoted tissue lysates were snap frozen in liquid nitrogen and stored at −80 °C.

■ ASSOCIATED CONTENT

Supporting Information

The Supporting Information is available free of charge at https://pubs.acs.org/doi/10.1021/acsomega.4c04457.

B3LYP optimized ligand structures; tables of ligand singlet and triplet excited states calculated with open and closed shell TD-CAMB3LYP methods; TEM images of NPs after ligand exchange; DLS distributions of control and ligand-sensitized NPs; excitation−emission matrices from NPs synthesized under air and argon; and emission decay fits for the luminescence lifetime measurements (PDF)

■ AUTHOR INFORMATION

Corresponding Author

Forrest M. Kievit − *Department of Biological Systems Engineering, University of Nebraska-Lincoln, Lincoln, Nebraska 68583, United States;* orcid.org/0000-0002-9847-783X; Email: fkievit2@unl.edu

Authors

Hunter A. Miller − *Department of Biological Systems Engineering, University of Nebraska-Lincoln, Lincoln, Nebraska 68583, United States;* orcid.org/0000-0001-6661-7458

Jessica Q. Wallace − *Department of Chemistry, University of Nevada, Reno, Reno, Nevada 89557, United States*

Hui Li − *Department of Chemistry, University of Nebraska-Lincoln, Lincoln, Nebraska 68588, United States;* orcid.org/0000-0003-0580-7033

Xing-Zhong Li − *Nebraska Center for Materials and Nanoscience, University of Nebraska-Lincoln, Lincoln, Nebraska 68588, United States*

Ana de Bettencourt-Dias − *Department of Chemistry, University of Nevada, Reno, Reno, Nevada 89557, United States;* orcid.org/0000-0001-5162-2393

Complete contact information is available at: https://pubs.acs.org/10.1021/acsomega.4c04457

Author Contributions

This manuscript was written with contributions from all authors. All authors approved the final version of the manuscript.

Funding

We acknowledge grant funding from the National Institute of Neurological Disorders and Stroke of the National Institutes of Health (R01NS109488) to F.K. This investigation is solely the responsibility of the authors and does not necessarily represent the official views of NINDS and NIH. AdBD acknowledges financial support through the National Science Foundation (CHE-2155047).

Notes

The authors declare no competing financial interest.

■ ACKNOWLEDGMENTS

The quantum chemical calculations were performed with the resources at the Holland Computing Center of the University of Nebraska, which receives support from the UNL Office of Research and Economic Development, and the Nebraska Research Initiative. The research was performed in part in the Nebraska Nanoscale Facility: National Nanotechnology Coordinated Infrastructure and the Nebraska Center for Materials and Nanoscience (and/or NERCF), which are supported by the National Science Foundation under Award ECCS: 2025298, and the Nebraska Research Initiative. The authors thank Brandon Z. McDonald for preparing tissue lysates and William Duralia for assisting in the data processing of excitation−emission matrices.

■ REFERENCES

(1) Furtado, D.; Bjornmalm, M.; Ayton, S.; Bush, A. I.; Kempe, K.; Caruso, F. Overcoming the Blood-Brain Barrier: The Role of Nanomaterials in Treating Neurological Diseases. *Adv. Mater.* **2018**, *30* (46), No. e1801362.

(2) Lee, Y.; Thompson, D. H. Stimuli-responsive liposomes for drug delivery. *Wiley Interdiscip. Rev.: Nanomed. Nanobiotechnol* **2017**, *9*(5) e1450..

(3) Singh, R.; Lillard, J. W., Jr. Nanoparticle-based targeted drug delivery. *Exp. Mol. Pathol.* **2009**, *86* (3), 215−323.

(4) Malam, Y.; Loizidou, M.; Seifalian, A. M. Liposomes and nanoparticles: nanosized vehicles for drug delivery in cancer. *Trends Pharmacol. Sci.* **2009**, *30* (11), 592−599.

(5) Joo, J.; Kwon, E. J.; Kang, J.; Skalak, M.; Anglin, E. J.; Mann, A. P.; Ruoslahti, E.; Bhatia, S. N.; Sailor, M. J. Porous silicon-graphene oxide core-shell nanoparticles for targeted delivery of siRNA to the injured brain. *Nanoscale Horiz.* **2016**, *1* (5), 407−414.

(6) Guo, X.; Deng, G.; Liu, J.; Zou, P.; Du, F.; Liu, F.; Chen, A. T.; Hu, R.; Li, M.; Zhang, S.; Tang, Z.; Han, L.; Liu, J.; Sheth, K. N.; Chen, Q.; Gou, X.; Zhou, J. Thrombin-Responsive, Brain-Targeting Nanoparticles for Improved Stroke Therapy. *ACS Nano* **2018**, *12* (8), 8723−8732.

(7) Sun, T.; Zhang, Y. S.; Pang, B.; Hyun, D. C.; Yang, M.; Xia, Y. Engineered nanoparticles for drug delivery in cancer therapy. *Angew. Chem., Int. Ed. Engl.* **2014**, *53* (46), 12320−12364.
(8) Bharadwaj, V. N.; Rowe, R. K.; Harrison, J.; Wu, C.; Anderson, T. R.; Lifshitz, J.; Adelson, P. D.; Kodibagkar, V. D.; Stabenfeldt, S. E. Blood-brainbarrier disruption dictates nanoparticle accumulation following experimental brain injury. *Nanomedicine* **2018**, *14* (7), 2155−2166.
(9) Zinger, A.; Soriano, S.; Baudo, G.; De Rosa, E.; Taraballi, F.; Villapol, S. Biomimetic Nanoparticles as a Theranostic Tool for Traumatic Brain Injury. *Adv. Funct. Mater.* **2021**, *31* (30), 2100722.
(10) Tarudji, A. W.; Miller, H. A.; Curtis, E. T.; Porter, C. L.; Madsen, G. L.; Kievit, F. M. Sex-based differences of antioxidant enzyme nanoparticle effects following traumatic brain injury. *J. Controlled Release* **2023**, *355*, 149−159.
(11) Wegner, K. D.; Hildebrandt, N. Quantum dots: bright and versatile in vitro and in vivo fluorescence imaging biosensors. *Chem. Soc. Rev.* **2015**, *44* (14), 4792−4834.
(12) Simonsen, J. B.; Kromann, E. B. Pitfalls and opportunities in quantitative fluorescence-based nanomedicine studies - A commentary. *J. Controlled Release* **2021**, *335*, 660−667.
(13) Chen, F.; Chen, M.; Yang, C.; Liu, J.; Luo, N.; Yang, G.; Chen, D.; Li, L. Terbium-doped gadolinium oxide nanoparticles prepared by laser ablation in liquid for use as a fluorescence and magnetic resonance imaging dual-modal contrast agent. *Phys. Chem. Chem. Phys.* **2015**, *17* (2), 1189−1196.
(14) Bazzi, R.; Flores-Gonzalez, M. A.; Louis, C.; Lebbou, K.; Dujardin, C.; Brenier, A.; Zhang, W.; Tillement, O.; Bernstein, E.; Perriat, P. Synthesis and luminescent properties of sub-5-nm lanthanide oxides nanoparticles. *J. Lumin.* **2003**, *102*−*103*, 445−450.
(15) Zhang, Y.; Hong, G.; Zhang, Y.; Chen, G.; Li, F.; Dai, H.; Wang, Q. Ag2S quantum dot: a bright and biocompatible fluorescent nanoprobe in the second near-infrared window. *ACS Nano* **2012**, *6* (5), 3695−3702.
(16) Davis, A. S.; Richter, A.; Becker, S.; Moyer, J. E.; Sandouk, A.; Skinner, J.; Taubenberger, J. K. Characterizing and diminishing autofluorescence in formalin-fixed paraffin-embedded human respiratory tissue. *J. Histochem. Cytochem.* **2014**, *62* (6), 405−423.
(17) Gerdes, M. J.; Sevinsky, C. J.; Sood, A.; Adak, S.; Bello, M. O.; Bordwell, A.; Can, A.; Corwin, A.; Dinn, S.; Filkins, R. J.; et al. Highly multiplexed single-cell analysis of formalin-fixed, paraffin-embedded cancer tissue. *Proc. Natl. Acad. Sci. U.S.A.* **2013**, *110* (29), 11982−11987.
(18) Zhao, J.; Zhong, D.; Zhou, S. NIR-I-to-NIR-II fluorescent nanomaterials for biomedical imaging and cancer therapy. *J. Mater. Chem. B* **2018**, *6* (3), 349−365.
(19) Elson, D.; Requejo-Isidro, J.; Munro, I.; Reavell, F.; Siegel, J.; Suhling, K.; Tadrous, P.; Benninger, R.; Lanigan, P.; McGinty, J.; Talbot, C.; Treanor, B.; Webb, S.; Sandison, A.; Wallace, A.; Davis, D.; Lever, J.; Neil, M.; Phillips, D.; Stamp, G.; French, P. Time-domain fluorescence lifetime imaging applied to biological tissue. *Photochem. Photobiol. Sci.* **2004**, *3* (8), 795−801.
(20) de Bettencourt-Dias, A.; Rossini, J. S. K. Ligand Design for Luminescent Lanthanide-Containing Metallopolymers. *Inorg. Chem.* **2016**, *55* (20), 9954−9963.
(21) Pal, R.; Parker, D.; Costello, L. C. A europium luminescence assay of lactate and citrate in biological fluids. *Org. Biomol. Chem.* **2009**, *7* (8), 1525−1528.
(22) dos Santos, C. M.; Harte, A. J.; Quinn, S. J.; Gunnlaugsson, T. Recent developments in the field of supramolecular lanthanide luminescent sensors and self-assemblies. *Coord. Chem. Rev.* **2008**, *252* (23−24), 2512−2527.
(23) Bunzli, J. C. Lanthanide luminescence for biomedical analyses and imaging. *Chem. Rev.* **2010**, *110* (5), 2729−2755.
(24) Wen, S.; Zhou, J.; Zheng, K.; Bednarkiewicz, A.; Liu, X.; Jin, D. Advances in highly doped upconversion nanoparticles. *Nat. Commun.* **2018**, *9* (1), 2415.
(25) Agbo, P.; Abergel, R. J. Ligand-Sensitized Lanthanide Nanocrystals: Merging Solid-State Photophysics and Molecular Solution Chemistry. *Inorg. Chem.* **2016**, *55* (20), 9973−9980.
(26) Amoroso, A. J.; Burrows, M. W.; Haigh, R.; Hatcher, M.; Jones, M.; Kynast, U.; Malik, K. M. A.; Sendor, D. The synthesis and characterisation of europium terpyridine-N-oxide complexes. *Dalton Trans.* **2007**, *16* (16), 1630−1638.
(27) de Bettencourt-Dias, A.; Bauer, S.; Viswanathan, S.; Maull, B. C.; Ako, A. M. Unusual nitro-coordination of europium(iii) and terbium(iii) with pyridinyl ligands. *Dalton Trans.* **2012**, *41* (36), 11212−11218.
(28) Edwards, A.; Claude, C.; Sokolik, I.; Chu, T. Y.; Okamoto, Y.; Dorsinville, R. Photoluminescence and electroluminescence of new lanthanide-(methyoxybenzoyl)benzoate complexes. *J. Appl. Phys.* **1997**, *82* (4), 1841−1846.
(29) Viswanathan, S.; de Bettencourt-Dias, A. Eu(III) and Tb(III) Luminescence Sensitized by Thiophenyl-Derivatized Nitrobenzoato Antennas. *Inorg. Chem.* **2006**, *45* (25), 10138−10146.
(30) Deng, H.; Chen, F.; Yang, C.; Chen, M.; Li, L.; Chen, D. Effect of Eu doping concentration on fluorescence and magnetic resonance imaging properties of Gd(2)O(3):Eu(3+) nanoparticles used as dual-modal contrast agent. *Nanotechnology* **2018**, *29* (41), 415601.
(31) Bazzi, R.; Flores, M. A.; Louis, C.; Lebbou, K.; Zhang, W.; Dujardin, C.; Roux, S.; Mercier, B.; Ledoux, G.; Bernstein, E.; Perriat, P.; Tillement, O. Synthesis and properties of europium-based phosphors on the nanometer scale: Eu2O3, Gd2O3:Eu, and Y2O3:Eu. *J. Colloid Interface Sci.* **2004**, *273* (1), 191−197.
(32) Mai, H.-X.; Zhang, Y.-W.; Si, R.; Yan, Z.-G.; Sun, L.-d.; You, L.-P.; Yan, C.-H. High-Quality Sodium Rare-Earth Fluoride Nanocrystals: Controlled Synthesis and Optical Properties. *J. Am. Chem. Soc.* **2006**, *128* (19), 6426−6436.
(33) Beeby, A. M.; Clarkson, I. M.; Dickins, R.; Faulkner, S.; Parker, D.; Royle, L.; de Sousa, A. S.; Williams, J. A. G.; Woods, M. Non-radiative deactivation of the excited states of europium, terbium and ytterbium complexes by proximate energy-matched OH, NH and CH oscillators: an improved luminescence method for establishing solution hydration states. *J. Chem. Soc., Perkin Trans.* **1999**, *2* (3), 493−504.
(34) Zhang, J.; Shade, C. M.; Chengelis, D. A.; Petoud, S. A Strategy to Protect and Sensitize Near-Infrared Luminescent Nd3+ and Yb3+: Organic Tropolonate Ligands for the Sensitization of Ln3+-Doped NaYF4 Nanocrystals. *J. Am. Chem. Soc.* **2007**, *129* (48), 14834−14835.
(35) Liang, T.; Wang, Q.; Li, Z.; Wang, P.; Wu, J.; Zuo, M.; Liu, Z. Removing the Obstacle of Dye-Sensitized Upconversion Luminescence in Aqueous Phase to Achieve High-Contrast Deep Imaging In Vivo. *Adv. Funct. Mater.* **2020**, *30* (16), 1910765.
(36) Wu, X.; Zhang, Y.; Takle, K.; Bilsel, O.; Li, Z.; Lee, H.; Zhang, Z.; Li, D.; Fan, W.; Duan, C.; Chan, E. M.; Lois, C.; Xiang, Y.; Han, G. Dye-Sensitized Core/Active Shell Upconversion Nanoparticles for Optogenetics and Bioimaging Applications. *ACS Nano* **2016**, *10* (1), 1060−1066.
(37) Cheignon, C.; Kassir, A. A.; Soro, L. K.; Charbonniere, L. J. Dye-sensitized lanthanide containing nanoparticles for luminescence based applications. *Nanoscale* **2022**, *14* (38), 13915−13949.
(38) Medina-Tato, S. B.; Armenta-Jaime, E.; Bélanger-Desmarais, N.; Ruiz-Ruiz, V. F.; Harris, J. P.; Reber, C.; Castillo-Blum, S. E. Luminescent lanthanide oxides nanoparticles with a surface agent acting as a sensitiser. *J. Phys. Chem. Solids* **2023**, *172*, 111048.
(39) Truillet, C.; Lux, F.; Brichart, T.; Lu, G. W.; Gong, Q. H.; Perriat, P.; Martini, M.; Tillement, O. Energy transfer from pyridine molecules towards europium cations contained in sub 5-nm Eu2O3 nanoparticles: Can a particle be an efficient multiple donor-acceptor system? *J. Appl. Phys.* **2013**, *114* (11), 114308.
(40) Liu, X.; Wu, W.; Cui, D.; Chen, X.; Li, W. Functional Micro-/Nanomaterials for Multiplexed Biodetection. *Adv. Mater.* **2021**, *33* (30), 2004734.

https://doi.org/10.1021/acsomega.4c04457
ACS Omega 2024, 9, 31093−31104

(41) Bettencourt-Dias, A. Small Molecule Luminescent Lanthanide Ion Complexes Photophysical Characterization and Recent Developments. *Curr. Org. Chem.* **2007**, *11*, 1460−1480.
(42) de Bettencourt-Dias, A. *Luminescence of Lanthanide Ions in Coordination Compounds and Nanomaterials*; John Wiley & Sons, 2014.
(43) Choppin, G. R. Factors in Ln(III) complexation. *J. Alloys Compd.* **1997**, *249* (1−2), 1−8.
(44) Söderlind, F.; Pedersen, H.; Petoral, R. M.; Käll, P. O.; Uvdal, K. Synthesis and characterisation of Gd2O3 nanocrystals functionalised by organic acids. *J. Colloid Interface Sci.* **2005**, *288* (1), 140−148.
(45) Tegafaw, T.; Liu, Y.; Ho, S. L.; Liu, S.; Ahmad, M. Y.; Al Saidi, A. K. A.; Zhao, D.; Ahn, D.; Nam, H.; Chae, W.-S.; Nam, S.-W.; Chang, Y.; Lee, G. H. High-Quantum-Yield Ultrasmall Ln2O3 (Ln = Eu, Tb, or Dy) Nanoparticle Colloids in Aqueous Media Obtained via Photosensitization. *Langmuir* **2023**, *39* (43), 15338−15342.
(46) Gao, J.; Li, Q.; Wang, C.; Tan, H. Ratiometric detection of hydroxy radicals based on functionalized europium(III) coordination polymers. *Mikrochim. Acta* **2017**, *185* (1), 9.
(47) Zhang, X.-T.; Fan, L.-M.; Fan, W.-L.; Li, B.; Liu, G.-Z.; Liu, X.-Z.; Zhao, X. A Series of Lanthanide Coordination Polymers Based on Designed Bifunctional 1,4-Bis(imidazol-1-yl)terephthalic Acid Ligand: Structural Diversities, Luminescence, and Magnetic Properties. *Cryst. Growth Des.* **2016**, *16* (7), 3993−4004.
(48) Zhao, X.; Huang, K.; Liu, Z.; Jiao, F.; Li, Z.; Hu, S. Synthesis and luminescent properties of Eu (III) complexes of 2-thienyltrifluoroacetonate, terephthalic acid and trioctylphosphine oxide. *J. Alloys Compd.* **2007**, *437* (1−2), 254−259.
(49) Kalinovskaya, I. V. Luminescent Europium(III) Compounds with Quinaldic Acid. *Russ. J. Appl. Chem.* **2023**, *96* (1), 21−26.
(50) Chen, J.; Meng, Q.; May, P. S.; Berry, M. T.; Lin, C. Sensitization of Eu3+ Luminescence in Eu:YPO4 Nanocrystals. *J. Phys. Chem. C* **2013**, *117* (11), 5953−5962.
(51) Socrates, G. *Infrared and Raman Characteristic Group Frequencies: Tables and Charts*; Wiley, 2004.
(52) Latva, M.; Takalo, H.; Mukkala, V.-M.; Matachescu, C.; Rodríguez-Ubis, J. C.; Kankare, J. Correlation between the lowest triplet state energy level of the ligand and lanthanide(III) luminescence quantum yield. *J. Lumin.* **1997**, *75* (2), 149−169.
(53) Zhang, Z.; He, L.; Feng, J.; Liu, X.; Zhou, L.; Zhang, H. Unveiling the Relationship between Energy Transfer and the Triplet Energy Level by Tuning Diarylethene within Europium(III) Complexes. *Inorg. Chem.* **2020**, *59* (1), 661−668.
(54) Huang, Y.-J.; Ke, C.; Fu, L.-M.; Li, Y.; Wang, S.-F.; Ma, Y.-C.; Zhang, J.-P.; Wang, Y. Excitation Energy-Transfer Processes in the Sensitization Luminescence of Europium in a Highly Luminescent Complex. *ChemistryOpen* **2019**, *8* (3), 388−392.
(55) Yang, C.; Fu, L.-M.; Wang, Y.; Zhang, J.-P.; Wong, W.-T.; Ai, X.-C.; Qiao, Y.-F.; Zou, B.-S.; Gui, L.-L. A Highly Luminescent Europium Complex Showing Visible-Light-Sensitized Red Emission: Direct Observation of the Singlet Pathway. *Angew. Chem., Int. Ed.* **2004**, *43* (38), 5010−5013.
(56) Alaoui, I. M. Nonparticipation of the Ligand's First Triplet State in Intramolecular Energy Transfer in Eu3+ and Tb3+ Ruhemann's Purple Complexes. *J. Phys. Chem.* **1995**, *99* (35), 13280−13282.
(57) Manzur, J.; Fuentealba, P.; Gil, Y.; Pérez-Obando, J.; Morales Alfaro, J.; Vega Carvallo, A. I.; Aravena, D.; Santana, R. C. d.; Carneiro Neto, A. N.; Spodine, E. Tuning the Emission of Homometallic DyIII, TbIII, and EuIII 1-D Coordination Polymers with 2,6-Di(1H-1,2,4-triazole-1-yl-methyl)-4-R-phenoxo Ligands: Sensitization through the Singlet State. *Inorg. Chem.* **2023**, *62* (47), 19195−19207.
(58) Hooda, A.; Khatkar, S. P.; Khatkar, A.; Malik, R. K.; Devi, S.; Dalal, J.; Taxak, V. B. Combustion synthesis, Judd-Ofelt parameters and optical properties of color tunable Ba3Y4O9: Eu3+ nanophosphor for near-UV based WLEDs. *J. Mater. Sci.: Mater. Electron.* **2019**, *30* (9), 8751−8762.
(59) Xia, T.; Shao, Z.; Yan, X.; Liu, M.; Yu, L.; Wan, Y.; Chang, D.; Zhang, J.; Zhao, D. Tailoring the triplet level of isomorphic Eu/Tb mixed MOFs for sensitive temperature sensing. *Chem. Commun.* **2021**, *57* (25), 3143−3146.
(60) Steemers, F. J.; Verboom, W.; Reinhoudt, D. N.; van der Tol, E. B.; Verhoeven, J. W. New Sensitizer-Modified Calix[4]arenes Enabling Near-UV Excitation of Complexed Luminescent Lanthanide Ions. *J. Am. Chem. Soc.* **1995**, *117* (37), 9408−9414.
(61) Shi, M.; Li, F.; Yi, T.; Zhang, D.; Hu, H.; Huang, C. Tuning the Triplet Energy Levels of Pyrazolone Ligands to Match the 5D0 Level of Europium(III). *Inorg. Chem.* **2005**, *44* (24), 8929−8936.
(62) Aebischer, A.; Gumy, F.; Bunzli, J. C. Intrinsic quantum yields and radiative lifetimes of lanthanide tris(dipicolinates). *Phys. Chem. Chem. Phys.* **2009**, *11* (9), 1346−1353.
(63) Wang, F.; Wang, J.; Liu, X. Direct evidence of a surface quenching effect on size-dependent luminescence of upconversion nanoparticles. *Angew. Chem., Int. Ed. Engl.* **2010**, *49* (41), 7456−7460.
(64) Petry, J.; Komban, R.; Gimmler, C.; Weller, H. Simple one pot synthesis of luminescent europium doped yttrium oxide Y(2)O(3):Eu nanodiscs for phosphor converted warm white LEDs. *Nanoscale Adv.* **2022**, *4* (3), 858−864.
(65) Johnson, N. J.; He, S.; Diao, S.; Chan, E. M.; Dai, H.; Almutairi, A. Direct Evidence for Coupled Surface and Concentration Quenching Dynamics in Lanthanide-Doped Nanocrystals. *J. Am. Chem. Soc.* **2017**, *139* (8), 3275−3282.
(66) Plancque, G.; Moulin, V.; Toulhoat, P.; Moulin, C. Europium speciation by time-resolved laser-induced fluorescence. *Anal. Chim. Acta* **2003**, *478* (1), 11−22.
(67) Ansari, A.; Dey, S.; Mohanta, D. Significant red-luminescence from citrate-gel and hydrothermally derived nanoscale Eu3+: Gd2O3 with alkali metal ion (Na+, K+) co-doping. *Bull. Mater. Sci.* **2022**, *45* (1), 21.
(68) Xia, J.; Zhao, B.; Wang, H.-S.; Shi, W.; Ma, Y.; Song, H.-B.; Cheng, P.; Liao, D.-Z.; Yan, S.-P. Two- and Three-Dimensional Lanthanide Complexes: Synthesis, Crystal Structures, and Properties. *Inorg. Chem.* **2007**, *46* (9), 3450−3458.
(69) Kirby, A. F.; Foster, D.; Richardson, F. S. Comparison of 7FJ← 5DO emission spectra for Eu(III) in crystalline environments of octahedral, near-octahedral, and trigonal symmetry. *Chem. Phys. Lett.* **1983**, *95* (6), 507−512.
(70) Li, S. W.; Ren, H. J.; Ju, S. G. Sensitized luminescence of LaF3: Eu3+ nanoparticles through pyromellitic acid. *J. Nanosci. Nanotechnol.* **2014**, *14* (5), 3677−3682.
(71) Dalal, J.; Dalal, M.; Devi, S.; Chahar, S.; Hooda, A.; Khatkar, A.; Malik, R.; Taxak, V.; Khatkar, S. Ba5Zn4Gd8O21: Tb3+—structural characterization and the Judd-Ofelt parameterization from emission spectra. *Methods Appl. Fluoresc.* **2020**, *8* (3), 035002.
(72) Wu, J.; Shi, S.; Wang, X.; Li, J.; Zong, R.; Chen, W. Controlled synthesis and optimum luminescence of Sm 3+-activated nano/submicroscale ceria particles by a facile approach. *J. Mater. Chem. C* **2014**, *2* (15), 2786−2792.
(73) Phogat, P.; Khatkar, S.; Taxak, V.; Malik, R. Eu3+ incorporated Bi4MgO4 (PO4) 2: Derivation of the novel nanophosphor by solution combustion and investigation in to crystallographic and photometric characteristics. *Solid State Sci.* **2022**, *124*, 106799.
(74) Xu, H.; Han, S.; Deng, R.; Su, Q.; Wei, Y.; Tang, Y.; Qin, X.; Liu, X. Anomalous upconversion amplification induced by surface reconstruction in lanthanide sublattices. *Nat. Photonics* **2021**, *15* (10), 732−737.
(75) Tilney, J. A.; Sørensen, T. J.; Burton-Pye, B. P.; Faulkner, S. Self-assembly between dicarboxylate ions and a binuclear europium complex: formation of stable adducts and heterometallic lanthanide complexes. *Dalton Trans.* **2011**, *40* (45), 12063−12066.
(76) de Bettencourt-Dias, A. Isophthalato-based 2D coordination polymers of Eu (III), Gd (III), and Tb (III): Enhancement of the terbium-centered luminescence through thiophene derivatization. *Inorg. Chem.* **2005**, *44* (8), 2734−2741.

https://doi.org/10.1021/acsomega.4c04457
ACS Omega 2024, 9, 31093−31104

(77) Bettencourt Dias, A. d.; Viswanathan, S. Luminescent Ln3+ nitrobenzoato complexes: first examples of sensitization of green and red emission. *Chem. Commun.* **2004**, No. 8, 1024−1025.
(78) Buenzli, J. C. G.; Yersin, J. R. Fluorescence spectra and lifetime measurements of aqueous solutions of europium nitrate and perchlorate. *Inorg. Chem.* **1979**, *18* (3), 605−607.
(79) Barik, P.; Verma, A.; Kumar, R.; Kumar, V.; Sahu, I. P. Structural and photoluminescence properties of europium (III)-activated lithium meta-silicate phosphors for solid-state lighting. *Appl. Phys. A: Mater. Sci. Process.* **2023**, *129* (10), 677.
(80) Johnson, K. R.; de Bettencourt-Dias, A. 1O2 generating luminescent lanthanide complexes with 1, 8-naphthalimide-based sensitizers. *Inorg. Chem.* **2019**, *58* (19), 13471−13480.
(81) Johnson, K. R.; Gracia-Nava, M. A.; de Bettencourt-Dias, A. Thiophene-derivatized pyridine-biscarboxamide as a sensitizer for LnIII luminescence and 1O2 generation. *J. Lumin.* **2020**, *224*, 117309.
(82) Ko, C.-C.; Yam, V. W.-W. Coordination compounds with photochromic ligands: ready tunability and visible light-sensitized photochromism. *Acc. Chem. Res.* **2018**, *51* (1), 149−159.
(83) Xiaochun, W.; Yongliang, Z.; Lianmeng, W.; Mei, Z.; Deqing, G. Synthesis and fluorescence properties of europium, terbium doped Zn2+, Cd2+ and Cr3+ complexes. *J. Rare Earths* **2007**, *25* (6), 679−683.
(84) Irfanullah, M.; Sharma, D. K.; Chulliyil, R.; Chowdhury, A. Europium-doped LaF 3 nanocrystals with organic 9-oxidophenalenone capping ligands that display visible light excitable steady-state blue and time-delayed red emission. *Dalton Trans.* **2015**, *44* (7), 3082−3091.
(85) Pacheco, M.; Chimeno-Trinchet, C.; Fernández-González, A.; Badía-Laíño, R. New europium-doped carbon nanoparticles showing long-lifetime photoluminescence: synthesis, characterization and application to the determination of tetracycline in waters. *Spectrochim. Acta, Part A* **2023**, *284*, 121756.
(86) Adusumalli, V. N.; Mrówczyńska, L.; Kwiatek, D.; Piosik, Ł.; Lesicki, A.; Lis, S. Ligand-Sensitised LaF3: Eu3+ and SrF2: Eu3+ Nanoparticles and in Vitro Haemocompatiblity Studies. *ChemMedChem* **2021**, *16* (10), 1640−1650.
(87) Feng, J.; Shan, G.; Maquieira, A.; Koivunen, M. E.; Guo, B.; Hammock, B. D.; Kennedy, I. M. Functionalized europium oxide nanoparticles used as a fluorescent label in an immunoassay for atrazine. *Anal. Chem.* **2003**, *75* (19), 5282−5286.
(88) Zhang, T.; Kitagawa, Y.; Moriake, R.; Ferreira da Rosa, P. P.; Islam, M. J.; Yoneda, T.; Inokuma, Y.; Fushimi, K.; Hasegawa, Y. Hybrid EuIII Coordination Luminophore Standing on Two Legs on Silica Nanoparticles for Enhanced Luminescence. *Chem.—Eur. J.* **2021**, *27* (58), 14438−14443.
(89) Varaksina, E. A.; Taydakov, I. V.; Ambrozevich, S. A.; Selyukov, A. S.; Lyssenko, K. A.; Jesus, L. T.; Freire, R. O. Influence of fluorinated chain length on luminescent properties of Eu3+ β-diketonate complexes. *J. Lumin.* **2018**, *196*, 161−168.
(90) Rastogi, C. K.; Saha, S.; Sivakumar, S.; Pala, R. G.; Kumar, J. Kinetically stabilized aliovalent europium-doped magnesium oxide as a UV sensitized phosphor. *Phys. Chem. Chem. Phys.* **2015**, *17* (6), 4600−4608.
(91) Khudoleeva, V. Y.; Utochnikova, V. V.; Kalyakina, A. S.; Deygen, I. M.; Shiryaev, A. A.; Marciniak, Ł.; Lebedev, V. A.; Roslyakov, I. V.; Garshev, A. V.; Lepnev, L. S.; Schepers, U.; Bräse, S.; Kuzmina, N. P. Surface modified EuxLa1-xF3 nanoparticles as luminescent biomarkers: Still plenty of room at the bottom. *Dyes Pigm.* **2017**, *143*, 348−355.
(92) Friedrich, S.; Sieber, C.; Drobot, B.; Tsushima, S.; Barkleit, A.; Schmeide, K.; Stumpf, T.; Kretzschmar, J. Eu(III) and Cm(III) Complexation by the Aminocarboxylates NTA, EDTA, and EGTA Studied with NMR, TRLFS, and ITC-An Improved Approach to More Robust Thermodynamics. *Molecules* **2023**, *28* (12), 4881.
(93) Li, X.-Z. New Features in Landyne 5−A Software Suite for Materials Characterization and Crystallography by Transmission Electron Microscopy. *Microsc. Microanal.* **2023**, *29* (Supplement_1), 737−738.
(94) Li, X. Z. Landyne−a Software Suite for Electron Diffraction Simulation and Analysis. *Microsc. Microanal.* **2016**, *22* (S3), 564−565.
(95) Schneider, C. A.; Rasband, W. S.; Eliceiri, K. W. NIH Image to ImageJ: 25 years of image analysis. *Nat. Methods* **2012**, *9* (7), 671−675.
(96) Ziegler, T.; Seth, M.; Krykunov, M.; Autschbach, J.; Wang, F. On the relation between time-dependent and variational density functional theory approaches for the determination of excitation energies and transition moments. *J. Chem. Phys.* **2009**, *130* (15), 154102.
(97) Casida, M. E.; Jamorski, C.; Casida, K. C.; Salahub, D. R. Molecular excitation energies to high-lying bound states from time-dependent density-functional response theory: Characterization and correction of the time-dependent local density approximation ionization threshold. *J. Chem. Phys.* **1998**, *108* (11), 4439−4449.
(98) Casida, M. E.; Chong, D. *Recent Advances in Density Functional Methods*; World Scientific: Singapore, 1995.
(99) Halgren, T. A. Merck molecular force field. V. Extension of MMFF94 using experimental data, additional computational data, and empirical rules. *J. Comput. Chem.* **1996**, *17* (5−6), 616−641.
(100) Halgren, T. A. Merck molecular force field. III. Molecular geometries and vibrational frequencies for MMFF94. *J. Comput. Chem.* **1996**, *17* (5−6), 553−586.
(101) Halgren, T. A. Merck molecular force field. II. MMFF94 van der Waals and electrostatic parameters for intermolecular interactions. *J. Comput. Chem.* **1996**, *17* (5−6), 520−552.
(102) Halgren, T. A.; Nachbar, R. B. Merck molecular force field. IV. Conformational energies and geometries for MMFF94. *J. Comput. Chem.* **1996**, *17* (5−6), 587−615.
(103) Lai, R.; Dodds, E. D.; Li, H. Molecular dynamics simulation of ion mobility in gases. *J. Chem. Phys.* **2018**, *148* (6), 064109.
(104) Becke, A. D. Density-functional thermochemistry. I. The effect of the exchange-only gradient correction. *J. Chem. Phys.* **1992**, *96* (3), 2155−2160.
(105) Tatewaki, H.; Koga, T. Contracted Gaussian-type basis functions revisited. *J. Chem. Phys.* **1996**, *104* (21), 8493−8499.
(106) Yanai, T.; Tew, D. P.; Handy, N. C. A new hybrid exchange-correlation functional using the Coulomb-attenuating method (CAM-B3LYP). *Chem. Phys. Lett.* **2004**, *393* (1−3), 51−57.
(107) Thellamurege, N. M.; Li, H. Note: FixSol solvation model and FIXPVA2 tessellation scheme. *J. Chem. Phys.* **2012**, *137* (24), 246101.
(108) Peach, M. J.; Benfield, P.; Helgaker, T.; Tozer, D. J. Excitation energies in density functional theory: an evaluation and a diagnostic test. *J. Chem. Phys.* **2008**, *128* (4), 044118.
(109) Eriksen, J. J.; Sauer, S. P. A.; Mikkelsen, K. V.; Christiansen, O.; Jensen, H. J. A.; Kongsted, J. Failures of TDDFT in describing the lowest intramolecular charge-transfer excitation in para-nitroaniline. *Mol. Phys.* **2013**, *111* (9−11), 1235−1248.
(110) Barca, G. M.; Bertoni, C.; Carrington, L.; Datta, D.; De Silva, N.; Deustua, J. E.; Fedorov, D. G.; Gour, J. R.; Gunina, A. O.; Guidez, E.; et al. Recent developments in the general atomic and molecular electronic structure system. *J. Chem. Phys.* **2020**, *152* (15), 154102.
(111) Thellamurege, N. M.; Si, D.; Cui, F.; Zhu, H.; Lai, R.; Li, H. *QuanPol: A Full Spectrum and Seamless QM/MM Program*; Wiley Online Library, 2013.

https://doi.org/10.1021/acsomega.4c04457
ACS Omega 2024, 9, 31093−31104